

PHYSICS-BASED SEA CLUTTER MODEL FOR IMPROVED DETECTION OF LOW RADAR CROSS-SECTION TARGETS

Brian O'Donnell, Richard LeBaron, Rodolfo Diaz, Antonia Papandreou-Suppappola

School of Electrical, Computer and Energy Engineering, Arizona State University, Tempe, AZ

ABSTRACT

This paper studies the challenging problem of detecting a low radar cross-section target in heavy sea clutter by proposing a physics-based sea clutter generation model. The model includes a process that generates random dynamic sea clutter based on the governing physics of water gravity and capillary waves and a finite-difference time-domain electromagnetics simulations process based on Maxwell's equations propagating the radar signal. A subspace clutter suppression detector is considered to remove dominant clutter eigenmodes. The improved detection performance over matched filtering is demonstrated using sea clutter model simulations.

1. MOTIVATION AND RELATION TO PRIOR WORK

The detection and tracking of small targets on the sea surface is difficult as strong scattering from the sea can mask weaker target reflections. In particular, at low grazing angles and high sea states, transmitted signals with bandwidths large enough to observe reflections from breaking waves and sea spikes can result in low signal-to-clutter ratios (SCRs) [1]. In such heavy sea clutter scenarios, the detection performance deteriorates and the targets cannot be realistically tracked. Increasing the received signal power through antenna gain, transmitter power, and pulse Doppler processing may not improve detection as sea clutter returns consist of the transmitted signal undergoing small Doppler shifts relative to the target.

One approach to improving target detection performance at low radar cross-section (RCS) is by accurately modeling the sea clutter statistics. This was demonstrated in prior work using the compound Gaussian model that relates back to the physical sea clutter phenomenology [2]. The model assumes that the sea clutter return consists of speckle and texture components. The speckle return is primarily a function of small-scale capillary waves forming a large number of independent scattering from the incident signal. The texture is a function of the large-scale gravity waves; it is assumed to modulate the local mean power of the speckle return, while exhibiting spatial correlation based on the range resolution, sea state, and wind speed [3]. The compound Gaussian model has been validated using real sea clutter data, and has been used to construct improved detectors and configure waveforms [4–6].

In our paper, we present a physics-based sea clutter generation model based on an electromagnetic simulation of gravity and capillary waves evolving through time. By computing radar returns from the simulated sea surface and low RCS target scattering, we utilize the statistical variation of the returns to separate the target from the clutter and thus improve target detection performance. We specifically compare the performance of a matched filter detector to that of a subspace clutter suppression detector [6]. The subspace clutter suppression detector is an eigenmode analysis algorithm that exploits the statistical independence of clutter compared to the target

of interest [7, 8]. As we demonstrate, this detector can separate and suppress clutter from the radar returns, significantly improving SCR and detection performance.

This paper is organized as follows. In Section 2, we propose the sea clutter generation model with the random dynamic sea surface and finite-difference time-domain simulations process models. Section 3 uses the sea clutter model to investigate the performance of a subspace clutter suppression detector. In Section 4, model parameters are varied to provide detection performance comparison results.

2. PHYSICS-BASED FDTD SEA CLUTTER SIMULATION

The sea clutter generation model includes two main processes. The first process is the generation of a three-dimensional (3D) random dynamic sea surface that moves according to the governing physics of water waves as driven by the wind; the waves include gravity waves whose restoring force is gravity, and capillary waves whose restoring force is water surface tension. The second process includes 2D finite-difference time-domain (FDTD) simulations. It is based on using Maxwell's equations to propagate radar pulses through the FDTD domain, where the incident electromagnetic (EM) field impinges on the sea surface and scatters. The implementation of a teleportation window [3] in the FDTD simulations separates the scattering field or clutter from the total field; it is then propagated to the far field and collected for processing. The 2D FDTD simulations involve individual radar pulses incident on single cuts of the dynamic 3D sea surface. The sea is modeled as a perfectly conducting surface (water cells are perfect electric conductors). As the radar pulse duration is on the order of ns, the surface is a static snapshot during each pulse simulation but is propagated in between simulations of subsequent pulses according to the pulse repetition time. For a single radar pulse, multiple down-wind cuts of the 3D sea surface are simulated. These cuts are strategically spaced in the cross-wind direction in an attempt to collect scattering samples of the 3D sea and capture scattering across the radar footprint area on the sea surface. The superposition of radar backscatter collected from the multiple down-wind sea cuts constitutes quasi-3D sea clutter. The features of the sea surface are developed in stages: incorporating 2D static gravity waves and developing a capillary waves model, implementing a spreading function to expand into 3D, and superimposing the capillary waves on the gravity waves while mathematically giving each random wave its respective phase velocity.

The gravity waves component of the 2D sea surface are generated as described in [9]. The height $f(y_n)$ of the 2D sea surface at points y_n along the surface is given by

$$f(y_n) = \frac{1}{L} \sum_{m=-N/2}^{N/2-1} F(K_m) \exp(jK_m y_n) \quad (1)$$

where $F(K_m) = \sqrt{2\pi L W(K_m)} R_m$, R_m is a zero-mean, unit-variance Gaussian random variable $r(0, 1)$ for $m=0, N/2$, and $R_m = ((r(0, 1) + jr(0, 1))/\sqrt{2})$ for $m=1, \dots, N/2 - 1$. The function $W(K_m) = (\alpha/(4|K_m|^3)) \exp(-\beta g^2/(K_m^2 U^4))$ is the

This work was supported by ONR and by a Doctoral Fellowship from the ASU Security and Defense Systems Initiative (SDSI) Institute.

Pierson-Moscowitz (P-M) sea spectrum [10], where L is the sea surface length in m, N is the number of surface sampling points, $K_n = 2\pi/\Lambda_n$ is the wave number of the ocean wave, Λ_n is the ocean wave wavelength, $\beta = 0.74$, $\alpha = 0.0081$, $g = 9.81 \text{ m/s}^2$ is the gravitational constant, and U is the wind speed in m/s.

The slope of the gravity waves versus time at any point on the sea surface is proportional to the amplitude modulation of the clutter (or the clutter texture) returning from that point of the sea, so it is vital that the instances of gravity waves are generated correctly. In order to verify that the gravity waves model is correct, we simulated 2D FDTD incident EM plane wave illumination on our gravity wave surface $f(y_n)$. The parameters of the EM simulations were chosen based on information found in previous work. The proper discretization of the P-M sea surface, to capture scattering from relevant details of the sea, is given in [11]. We chose an extreme case to reproduce for generating the far field scattering from large details of the sea (gravity waves), following an FDTD simulations study in [12]. The sea details of interest are relatively large gravity waves, with a sea state of 7 (wind speed of 20 m/s) and a significant wave height of roughly 6 m. Thus, to capture details of this size, the free space EM illumination wavelength is chosen as $\lambda_0 = 7.49 \text{ m}$. The sea surface is sampled at $\lambda_0/16$ intervals. The discretization cell in our FDTD space is $\lambda_0/16$, and the plane wave EM illumination angle of incidence is 20 degrees above the horizon. Using these settings, we simulated 40 independent, completely decorrelated, random instances of the gravity wave surface of total length $160\lambda_0 \text{ m}$.

The scattering from the gravity waves is propagated to the far field over the horizon, where evidence of the changing slopes of larger gravity waves can be seen from one instance of sea to the next. The far field scattered intensity of 3 instances and the average of 40 instances (black curve) are shown in Figure 1. These results

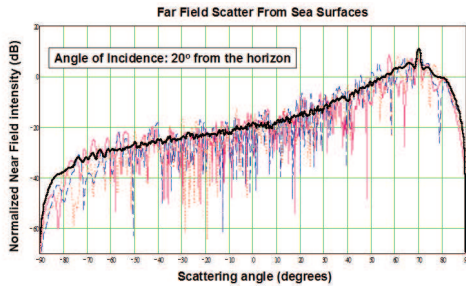


Fig. 1. Far field of 2D gravity waves.

demonstrate that we have a valid simulation of large realistic sea surface details in the EM environment using the FDTD computational EM method. The results also show that the 2D gravity wave surface is correctly generated.

To include the smaller details of the sea surface, we develop an energy spectrum to generate capillary waves in the same manner that the P-M spectrum is used to generate gravity waves. The spectrum is obtained using results from other capillary wave studies. We first estimate an exponential function that relates the wind speed U and capillary wave wavelength Λ [13]. The total kinetic and potential energy of water waves is given by $E = \rho\pi A^2$, where A is the wave amplitude and ρ is the density of water [14], and the amplitude of the capillary wave of greatest height is $2A = 0.73\Lambda$ [15]. Using these relations, we estimate the energy spectrum for capillary waves using $w(K_n) = (4\alpha_c\rho\pi^3U/|K_n|^2) \exp(-(K_B - \beta_c K_n)/(\beta_c^2 K_n))^2$, where $K_B = 2\pi/\Lambda_B$, Λ_B is the wavelength boundary between gravity and capillary waves, $\alpha_c = 0.0445$, and $\beta_c = 0.6$. This expression

does not account for other phenomena such as the effect of the local gravity wave slope and the angle of incidence of the local wind and instantaneous wind speed. However, it yields roughly the correct capillary wave heights based on experimental data [13] and is suitable for our study. Note that, although capillary and gravity waves are generated by the same approach, we continuously change the random number sets to prevent repeating capillary wave patterns.

The waves are propagated using the phase velocity equation [14]

$$v_p^2 = \frac{T}{\rho}K + \frac{g}{K}, \quad (2)$$

where T is the surface tension per length, ρ is the water mass density, g is gravity acceleration, $K = 2\pi/\Lambda$ is the water wave number, and Λ is the wavelength of the water wave. The first and second terms in (2) correspond to the velocity of capillary waves and gravity waves, respectively. Each wave is given a phase velocity $\phi_n = K_n y_n - \omega_n t$, following (2), where $\omega_n = (|K_n|^2(TK_n/\rho + g/K_n))^{0.5}$. To expand to 3D surface, we implement a spreading function as in [16]. Superimposing the moving capillary waves on the moving gravity waves results in the full dynamic and random 3D realistic sea surface.

The speckle component of sea clutter is backscatter from capillary waves. A simple test to demonstrate that our capillary waves scatter clutter in as similar fashion as the real sea is to calculate the Pearson's correlation coefficient of the first returning clutter pulse with all returning pulses. If the capillary waves have the correct motion, the speckle component of the clutter decorrelates in the time that real sea speckle decorrelates, which is on the order of 10 ms. For this test, in order to best observe the capillary waves, we chose to use X-band radar, since the EM wavelength is on the order of the capillary wave wavelength and amplitude. We simulated 100 radar pulses incident on a single cut of time-varying 3D sea, using 1 ms pulse repetition time, to capture the effect of the clutter. The correlation results are plotted in Figure 2, which shows that the speckle decorrelates in approximately 15 ms.

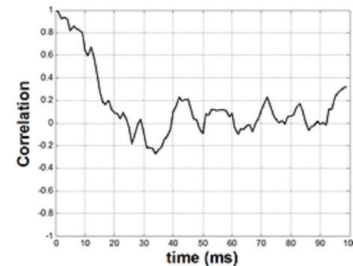


Fig. 2. Decorrelations of the radar returns from the simulated sea clutter occur over approximately 15 ms.

3. DETECTION METHODS

We consider a radar system for detecting a target in heavy sea clutter. The target is assumed to have low radar cross-section due to its actual size and its relative size in relation to the wavelength of the illuminating radar. We assume that the radar system transmits a pulse train of K identical pulses, $s(t)$, which scatter off sea surface scatterers, and if present, the target. The two detection hypotheses describing this scenario for the k th transmit signal, $k = 1, 2, \dots, K$, and the i th sea surface scatterer are given by

$$H_0 : x_k(t) = \sum_i a_{k,i} s(t - t_i) + w(t)$$

$$H_1 : x_k(t) = b_k s(t - t_0) + \sum_i a_{k,i} s(t - t_i) + w(t).$$

Under hypothesis H_0 , we assume that that received signal consists of multiple scatterers with complex scattering coefficients $a_{k,i}$ and time delays t_i and white Gaussian noise $w(t)$. Under hypothesis H_1 ,

we assume that, in addition to the scatterers and noise, the target is also present with a scattering coefficient b_k at time delay t_0 . In both hypotheses, the signals are sampled using as sampling period T_s to yield the discrete time sequence $x_k[n] = x_k(tT_s)$, $n = 0, \dots, N-1$. For the rest of the paper, we assume that the clutter-to-noise ratio is very high and that the effects of noise on detection can be ignored.

3.1. Generalized Matched Filter Detector

We derive the generalized matched filter (GMF) detector, that under hypothesis H_1 , assumes that the discrete-time incident signal $s[n]$ is known and deterministic but the target time-delay is unknown. After first estimating the time-delay using maximum likelihood estimation, the GMF detector is obtained by maximizing the probability of detection for a fixed false alarm rate. For our signal model, the discrete-time matched filter output corresponding to the k th pulse at the ℓ th lag, $\ell = 0, \dots, N-1$, with estimated n_0 , is given by

$$r_k[\ell] = b_k z_s[\ell - n_0] + \sum_{n=-(N-1)}^{N-1} z_s[n] d_k[n + \ell] \quad (3)$$

where the autocorrelation function of the transmit signal $s[n]$ at lag ℓ is defined as $z_s[\ell] = \sum_{n=0}^{N-1} s[n] s^*[n - \ell]$, and $d_k[\ell] = \sum_i a_{k,i}$ is the aggregate scattering coefficient from all of the clutter scatterers that fall within the ℓ th range bin. The decision threshold γ is set based on the distribution of $r_k[m]$ and by fixing either a desired value of false alarm rate \mathbf{P}_{FA} or probability of detection \mathbf{P}_{D} .

3.2. Subspace Clutter Suppression Detector

The GMF detector is not expected to perform well for low RCS targets in heavy sea clutter. In such cases, the clutter is much stronger than the signal, and for reasonable values of \mathbf{P}_{D} , the number of false alarms is large. This is expected as matched filtering does not involve clutter mitigation. The subspace clutter suppression (SCS) detector decomposes the signal into subspaces consisting of mostly clutter or mostly target energy. The detection performance is improved when only the subspaces that are orthogonal to the clutter are processed.

We assume a Swerling I point target so that the complex reflectivity $\mathbf{b} = [b_1 \ b_2 \ \dots \ b_K]^T$ of the target for all K transmit pulses has a zero-mean complex Gaussian distribution with covariance matrix $\sigma^2 \mathbf{I}_K$, where \mathbf{I}_K is the $(K \times K)$ identity matrix. For all K transmit pulses, the matched filter output at the ℓ th lag or range bin can be written in vector form as

$$\mathbf{r}_\ell = \mathbf{b} z_s[\ell - n_0] + \sum_{n=-(N-1)}^{N-1} \mathbf{d}_{n+\ell} z_s[n] \quad (4)$$

where $\mathbf{r}_\ell = [r_1[\ell] \ r_2[\ell] \ \dots \ r_K[\ell]]^T$, \mathcal{H} denotes complex transpose, and $\mathbf{d}_{n+\ell} = [a_{1,n+\ell} \ a_{2,n+\ell} \ \dots \ a_{K,n+\ell}]^T$. The covariance matrix of the matched filter output depends on both the target and clutter characteristics, and it is given by

$$\begin{aligned} \mathbf{R}_\ell &= E[\mathbf{r}_\ell \mathbf{r}_\ell^{\mathcal{H}}] = E[\mathbf{b} \mathbf{b}^{\mathcal{H}}] |z_s[\ell - n_0]|^2 \\ &+ \sum_{n=-(N-1)}^{N-1} \sum_{l=-(N-1)}^{N-1} E[\mathbf{d}_{n+\ell} \mathbf{d}_{l+\ell}^{\mathcal{H}}] z_s[\ell] z_s^{\mathcal{H}}[l]. \end{aligned}$$

The matrix can be re-written in the form of the compound Gaussian sea clutter model as

$$\mathbf{R}_\ell = \sigma^2 \mathbf{I}_K |z_s[\ell - n_0]|^2 + \sum_{n=-(N-1)}^{N-1} \Phi L_{n+\ell} |z_s[n]|^2 \quad (5)$$

where Φ is the speckle covariance matrix and L_ℓ is the sea clutter texture component.

Some existing detection methods use the above formulation to estimate the texture and speckle clutter components for use in a generalized likelihood ratio test. While a reasonable approach, estimating the texture and speckle clutter components is computationally intensive, and it is often performed using expectation maximization or another iterative method. A less computationally intensive approach, that also yields reasonably good results, estimates sample covariance matrix from the data in all the range bins in one coherent processing interval as

$$\mathbf{R} = \frac{1}{N} \sum_{\ell=0}^{N-1} (\mathbf{r}_\ell - \bar{\mathbf{r}}_\ell)(\mathbf{r}_\ell - \bar{\mathbf{r}}_\ell)^{\mathcal{H}} \quad (6)$$

where $\bar{\mathbf{r}}_\ell$ is the mean value of \mathbf{r}_ℓ at the ℓ th lag. To suppress the clutter from the received signal, we decompose \mathbf{R} into the eigenvector matrix \mathbf{Q} and diagonal eigenvalue matrix \mathbf{D} to obtain $\mathbf{R} = \mathbf{Q} \mathbf{D} \mathbf{Q}^{\mathcal{H}}$, where we assume that the eigenvalues along the diagonal of \mathbf{D} are sorted in descending order. The eigenvector matrix \mathbf{Q} is also sorted according to the ordered eigenvalue matrix.

Negative signal-to-clutter ratio (SCR) values imply that the larger eigenvalues and associated eigenvectors are due to sea clutter and define the eigenvectors that we want to suppress. We form a matrix \mathbf{Q}_c from the $J < K$ eigenvectors of \mathbf{Q} whose columns are associated with the smallest J eigenvalues of \mathbf{R} . The projected signal onto the signal subspace is given by $\mathbf{Q}_c \mathbf{Q}_c^{\mathcal{H}} \mathbf{r}_\ell$; this is the clutter suppressed signal that results in a larger SCR than \mathbf{r}_ℓ . Using the clutter suppressed signal for target detection results in an improved detection performance when compared to that of the GMF detector.

4. SIMULATION RESULTS

In order to evaluate the performance characteristics of the GMF and SCS detectors across a range of SCRs, we need to vary the strength of the clutter and target reflections. Varying these parameters is straightforward when clutter realizations are simulated using the compound Gaussian model or any other statistical model. However, this is not the case when using our proposed sea clutter generation model. The data generated from the physics-based FDTD model is controlled by physical properties of the sea surface (such as the size and shape of the waves), the target (such as the size of an object), and the radar (such as the radar beamwidth). While we have direct control over the strength of the clutter and target reflections, we do not know the exact numerical value of the SCR. This is because the reflected signal is a combination of both direct reflection from the target as well as delayed reflections from the sea surface; this makes it difficult to calculate just the target component or just the clutter component of the received signal.

As we cannot control the numerical SCR values, we cannot specify the exact detector performance, such as the probability of detection versus the probability of false alarm, for a given SCR. We can, however, evaluate the detector performance for relative ranges of SCR values, that is simulate scenarios for relatively larger or smaller SCRs. In order to accomplish this, we keep all parameters but one constant, and then we vary that one parameter to affect the SCR. In the following simulations, we hold the target size and radar beamwidth constant but increase the size of the waves resulting in varying SCR values. We consider three such scenarios to illustrate the detector performance across a wide range of SCRs. The first two scenarios show detection performance for negative SCR values: we denote the corresponding SCR values of the two scenario as SCR_1 and SCR_2 , respectively. We varied the parameters such that SCR_2 is lower than SCR_1 . The receiver-operating characteristic (ROC) curves, demonstrating probability of detection \mathbf{P}_{D} as a function of

the probability of false alarm P_{FA} , for the GMF and SCS detectors SCR_1 and SCR_2 are shown in Figure 3. As expected, the SCS detector outperforms the GMF detector. The other notable result is that, while increasing the SCR decreases the performance of both detectors, the performance of the SCS detector degrades at a slower rate than the GMF detector.

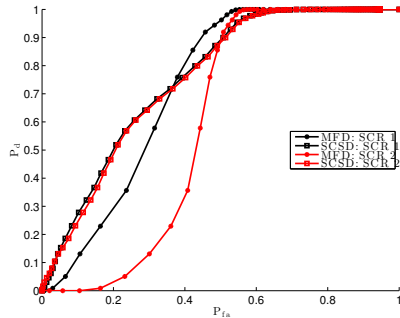


Fig. 3. ROC curves comparing the performance of the subspace clutter suppression (SCS) detector and the generalized matched filter (GMF) detector using $SCR_1 > SCR_2$.

In the third scenario, we used the positive SCR value SCR_3 and the ROC curves comparing the GMF and SCS detectors are shown in Figure 4. In this case, the detection performance of the GMFD is higher than the one for the SCS detector. Note that this result is expected since at higher SCR values, the largest eigenmode consist of target energy and not clutter; suppressing the largest eigenmodes results in decreasing the SCR and thus the SCR detector performance.

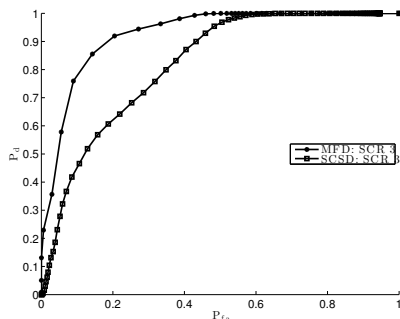


Fig. 4. ROC curves comparing the performance of the SCS and GMF detectors using SCR_3 value.

The simulated results shown in Figures 3 and 4 use the sea clutter generation model with $K=31$ pulses; for the SCS detector, only the first eigenmode was suppressed ($J=30$). The number of clutter eigenvectors is data dependent and is often chosen by looking for an abrupt drop-off value in the eigenvalue amplitude from the ordered list of eigenvalues. For $K=31$, this drop-off value occurred after only one eigenvalue. We expect that for larger values of K , more than one clutter eigenmode would need to be suppressed. However, as in this set of simulations we considered a constant pulse repetition frequency, larger values of K resulted in poorer detection statistics because the sample covariance matrix was then computed from decorrelated sea clutter data.

5. CONCLUSION

This paper proposed a novel sea clutter generation model for sea clutter using a 3D random dynamic sea surface with a capillary wave

model. The capillary wave model included capillary waves with gravity as the restoring force as well as capillary waves where the restoring force is the water surface tension. The generation model includes 2D finite-difference time-domain (FDTD) sea clutter simulations. We investigated a simple matched filter detector and a subspace clutter suppression detector, and we used the FDTD simulations to compare the performance of the two detectors.

6. REFERENCES

- [1] M. Skolnik, *Radar Handbook*. McGraw Hill, 2008.
- [2] S. Haykin, R. Bakker, and B. W. Currie, "Uncovering nonlinear dynamics - The case study of sea clutter," *Proceedings of the IEEE*, vol. 90, no. 5, pp. 860–881, 2002.
- [3] M. E. Watts and R. E. Diaz, "Perfect plane-wave injection into a finite FDTD domain through teleportation of fields," Arizona State University, Tech. Rep., 2003.
- [4] P. Stinco, M. Greco, and F. Gini, "Adaptive detection in compound-Gaussian clutter with inverse-gamma texture," in *IEEE Int. Conf. on Radar*, vol. 1, 2011, pp. 434–437.
- [5] F. Gini and A. Farina, "Vector subspace detection in compound-gaussian clutter. Part I: Survey and new results," *IEEE Transactions on Aerospace and Electronic Systems*, vol. 38, no. 4, pp. 1295–1311, 2002.
- [6] S. P. Sira, D. Cochran, A. Papandreou-Suppappola, D. Morrell, W. Moran, S. Howard, and R. Calderbank, "Adaptive waveform design for improved detection of low-RCS targets in heavy sea clutter," *IEEE Journal of Selected Topics in Signal Processing*, vol. 1, no. 1, pp. 56–66, 2007.
- [7] A. Suvorova, B. Moran, and M. Viola, "Adaptive modelling of sea clutter and detection of small targets in heavy clutter," in *International Radar Conference*, 2003, pp. 614–618.
- [8] A. Haimovich, "The eigencanceler: Adaptive radar by eigenanalysis methods," *IEEE Transactions on Aerospace and Electronic Systems*, vol. 32, no. 2, pp. 532–542, 1996.
- [9] E. Thorsos, "The validity of the kirchhoff approximation for rough surface scattering using a gaussian roughness spectrum," *J. Acoust. Soc. Amer*, vol. 83, p. 7892, 1988.
- [10] W. J. Pierson and L. Moskowitz, "A proposed spectral form for fully developed wind seas based on the similarity theory of S. A. Kitaigorodskii," *Journal of Geophysical Research*, vol. 69, no. 24, pp. 5181–5190, 1964.
- [11] J. V. Toporkov, R. T. Marchand, and G. S. Brown, "On the discretization of the integral equation describing scattering by rough conducting surfaces," *IEEE Transactions on Antennas and Propagation*, vol. 46, no. 1, pp. 150–161, 1998.
- [12] S. L. B. Frank D. Hastings, John B. Schneider, "A monte-carlo ftdt technique for rough surface scattering," *IEEE Trans. AP*, vol. 43, no. II, 1995.
- [13] L. C. Bobb, G. Ferguson, , and M. Rankin, "Capillary wave measurements," *Applied Optics*, vol. 18, pp. 1167–1171, 1979.
- [14] A. J. W. Sommerfeld, *Mechanics of Deformable Bodies*. Academic Press, 1950, vol. 2.
- [15] G. D. Crapper, "An exact solution for progressive capillary waves of arbitrary amplitude," *Journal of Fluid Mechanics*, vol. 2, pp. 532–540, 1957.
- [16] J. Frechot, "Realistic simulation of ocean surface using wave spectra," in *International Conference on Computer Graphics Theory and Applications*, 2006.